



This work was carried out in whole or in part within the framework of the NOMATEN Center of Excellence, supported from the European Union Horizon 2020 research and innovation programme (Grant Agreement No. 857470), the European Regional Development Fund via the Foundation for Polish Science International Research Agenda PLUS programme (Grant No. MAB PLUS/2018/8), *and the initiative of the Ministry of Science and Higher Education 'Support for the activities of Centers of Excellence established in Poland under the Horizon 2020 program' under agreement No. MEiN/2023/DIR/3795.*

This is the accepted manuscript submitted to: International Journal of Mechanical Sciences Volume 272, 15 June 2024, 109138, published on 27 February 2024 with the embargo period till: 27 February 2026.

DOI: 10.1016/j.ijmecsci.2024.109138

Size effects in spherical indentation of single crystal copper

S. Kucharski^{1a}, M. Maj^a, M. Rys^{b,a}, H. Petryk^a

^a*Institute of Fundamental Technological Research, Polish Academy of Sciences,
Pawińskiego 5B, 02-106 Warsaw, Poland*

^b*NOMATEN Centre of Excellence, National Centre for Nuclear Research, Soltana 7, Otwock, 05-400,
Poland*

Abstract

A comprehensive study of the size effects in the spherical indentation test of a copper single crystal is carried out. The main novelty of the approach is the analysis of a wide spectrum of parameters measured in the test that are predicted by the proposed model, and the prediction is verified experimentally for six different tip radii. Load-penetration depth curves, nominal hardness, pile-up and sink-in profiles, and the rotation and rotation gradient of the crystallographic lattice in the cross-section beneath the indenter have been measured and also calculated using 3D finite element simulations on the micro- and nanometer scale. Two gradient-effects are examined numerically within the Cosserat elastoplasticity framework with the gradient-enhanced hardening law. It is shown that a good prediction of the experimentally observed size effect on nominal hardness is achieved using the conventional power-hardening law, calibrated from the standard uniaxial compression test, enhanced with a term dependent on the lattice spin gradient term with no adjustable parameter. Furthermore, it has been found that the observed distribution of lattice rotation and decrease in the rotation magnitude with decreasing indenter radius can be qualitatively modelled by adjusting the coefficient of accumulated lattice curvature energy within the same framework.

Keywords: Hardness, Metals, Dislocations, Lattice rotation, Plasticity, Strain gradient, Nanoindentation

1. Introduction

The progress of modern technologies, like micro-forming or development of micro-electro-mechanical systems (MEMS), requires a better understanding of the behaviour of metallic materials at different scales. It is known that the deformation resistance of a material in the elastic-plastic state depends on the deformed volume or sample size. This topic was discussed extensively by Zhu et al. [1]. Two categories of size effect were distinguished: the intrinsic, which is an effect of microstructural constraints, and the extrinsic, resulting from dimensional constraints (e.g. sample size). The authors have classified indentation size effect (ISE) as the extrinsic size effect with three-dimensional constraints. However, the classification is more complex, since even for single crystals the hardness depends on both: the plastic strain gradient induced by the tip geometry and the effect of existing defect structures in the tested material [2].

A relatively simple indentation test can be carried out on a variety of scales as different amounts of material are involved in the test depending on the tip applied and the depth

¹Corresponding author S. Kucharski, email: skuchar@ippt.pan.pl

of penetration. The material response in such tests is known as the indentation size effect (ISE). As reviewed below, ISE has been investigated experimentally and numerically in numerous studies, but has not been yet sufficiently explored. Using the indentation and micro-pillar compression tests, Nix et al. [3] have shown the different mechanisms that are responsible on ISE, that is geometrically necessary dislocations (GNDs) at the micrometer scale, and dislocation starvation and nucleation at the nanometer scale. A valuable overview of ISE was provided by Pharr et al. [4].

The indentation size effect was basically modelled in relation to the increase of hardness with decreasing extrinsic length scale as in the well-known Nix-Gao model [5], which explains this behaviour by the material hardening due to the presence of GNDs. These dislocations are required to accommodate plastic strain gradients generated by indenter within the crystal. The model introduced a material length scale and was applied by many authors e.g. [6, 7, 8, 9, 10, 11, 12]. The Nix-Gao model was modified as in [13, 14] and extended to the isotropic, 3D, ‘mechanism-based’ model in FEM approach in which strain gradient was taken into account [15, 16]. The mechanism-based strain gradient crystal plasticity was applied to simulate ISE in FCC single crystal by Lee et al. [17]. In the model, the slip resistance of each slip system was modified due to density of GNDs, accordingly to intrinsic length scale coefficient. The indentation tests with conical and Berkovich tips were simulated and pile-up/sink-in pattern was taken into account in calculation of hardness. The comparison with experimental results published elsewhere was shown.

Validation of ISE models was initially limited to comparison of hardness values obtained from simulation and experiment e.g. [6, 7, 8, 9, 18]. The experimental values of hardness were usually determined without account for the complex shape of residual impressions resulting from the material anisotropy. In only a few papers, e.g. [19, 20, 21, 22] the contact area required for hardness calculation was estimated by measuring the residual imprint. Additionally, hardness was frequently the only quantity used to calibrate the model parameters. In few works, e.g. [23, 24], both hardness and GND density beneath the indent were estimated experimentally in order to confirm the predictions of the Nix-Gao model.

The models of crystal plasticity (referred to as CP), which take into account the anisotropy of single crystals, were used to model the indentation tests, although rarely with a strain-gradient enhancement (SGCP) to model ISE. They allowed insight into the deformation mechanisms of single crystals, which were examined using the indentation test. Thus, not only hardness but also other modelling results can be verified experimentally.

In the works discussed in the next paragraphs, the surface topography around the residual imprint and/or the lattice rotations beneath it were analysed and compared with experimental data. As commented below, on the basis of lattice rotation the density of GND was determined both in the experiment and in the simulation. However, the agreement between theoretical and experimental results was not satisfactory, even in those works where the size effect was not considered (this approach was presented in most of the papers cited). Other published papers also have certain limitations indicated below, which motivated this attempt at more comprehensive study.

The pile-up patterns and misorientation distributions around indents made with spherical tip on the sample surface were simulated by Wang et al. [25] using CP model (without size effect) for a copper single crystals with three crystallographic orientations. Only one level of load was taken into account and an experimental verification was limited

to comparison of contour plots of pile-up patterns. The lattice orientation below sphero-conical indent in the [111] oriented copper single crystal was investigated experimentally (EBSD in serial sections) and numerically (CP) by Zafaraani et al. [26]. The lattice rotations determined in experiments were smaller and show more complex patterns than those obtained in simulations; the changes of rotation fields in the experiment were more rapid. In the simulations, the largest rotations were observed in outer tangent zone, while in the inner zone, close to the indenter axis the rotation were smaller. Other simulation results like pile-up patterns or $P - h$ curves were not analysed. The load-penetration depth curves and topography of residual impression (pile-up patterns) obtained in experiments and in numerical simulations (CP model) were compared, e.g., in [27], [28] and [29].

The mechanically affected zone produced by scratch, impact and indentation tests conducted at macro-scale with a spherical tip or radius $R = 1.25$ mm in a copper single crystal was investigated by Juran et al. [30]. The lattice misorientations over the cross-section beneath the indent measured by EBSD and simulated numerically (CP model) were compared. The maximum misorientation values resulting from simulation and experiment were similar, but in the simulation the zone of large misorientation was more extended. The authors stated that a verification of the CP models can be performed on the basis of comparison of the load-penetration depth curve and lattice misorientation. However, the load-penetration curves and pile-up patterns were not provided.

Less numerous are the works in which SGCP model was applied to simulate spherical nanoindentation test. In the paper [31] the spherical nanoindentation in a copper single crystal was analysed experimentally and numerically (SGCP model). The maps of residual impressions, lattice rotation fields as well as GND densities beneath the indents obtained in the experiments and simulations were compared but the agreement was rather qualitative. In contrast, the simulated and experimental $P - h$ curves were very similar. Only one level of penetration depth ($h/R = 0.02$) and two tip radii ($7.4 \mu\text{m}$ and $27 \mu\text{m}$) were analysed. The authors concluded that the size effect cannot be explained by the hardening which results only from evolution of GND density and other hardening mechanisms should be taken into account (e.g. dislocation source activation).

The lattice rotation and pile-up pattern generated by nanoindentation in β -Ti alloy with a bcc structure was investigated numerically by Demiral et al. [32]. The 3D crystal plasticity finite element model with account for strain gradient was applied. Although sphero-conical tip with $1 \mu\text{m}$ radius was used, only spherical part was involved in the indentation ($h/R = 0.3$). It was shown that there is a correlation between lattice rotations and pile-up profiles, and that the high strain gradient is not necessarily associated with the lattice rotations. The effect of strain gradient on lattice rotations, GND density and pile-up pattern was discussed. However, the comparison of numerical results with experiment was limited to one pile-up profile and the agreement was rather poor, and the $P - h$ curves were not provided.

Load penetration curves and pile-up patterns produced in nanoindentation tests carried out with sphero-conical tip ($R = 5 \mu\text{m}$) on ARMCO iron under different loads were analysed by Engels et.al. [33]. The numerical simulation of the tests was performed using SGCP model. A satisfactory agreement of simulation results and experimental data was achieved for load-penetration curves, however for the pile-up profiles and hardness the consistency was much worse. The lattice rotations were not discussed.

The relationship between ISE and lattice rotations in a copper single crystal was investigated numerically by Gao et al. [34] using SGCP model. It was found that the lattice rotations depend on the crystallographic orientation, activated slip systems, the

indenter shape and the h/R ratio, but they are insensitive to the strain gradients. The latter influence the hardness and thus ISE. In the simulation of indentation tests four spherical tips ($R = 10, 15, 20, 100 \mu\text{m}$) were applied, but a very low penetration depth was assumed ($h/R = 0.008$). The experimental verification presented was very limited, only $P-h$ curves and lattice rotations for the greatest radius ($R = 100 \mu\text{m}$) were compared with experimental data.

Purely experimental investigations of the lattice rotations below and around indents made by sphero-conical tip ($R = 1 \mu\text{m}$) in the copper single crystal was presented by Demir et al., [24]. The GND densities below and around the indents were calculated on the basis of the orientation changes captured using EBSD in different cross-sections of the residual impressions. Four levels of indentation depth were applied to observe size effect. It was noted that GND density does not increase with the decrease of penetration depth and the increase of hardness. The authors conclude, that GND density does not directly contribute to the increase of hardness, and the latter is caused by the reduction in free dislocation segment length (limitation of dislocation sources) associated with the presence of GND. These non-conventional conclusions may be due to the fact that the authors applied a load range which is not typical neither for spherical nor for conical tips, i.e. h/R varies between 0.46 and 1.23. Therefore some of the examined indents correspond to a deep spherical indentation test and others correspond to shallow quasi-sharp indentation test, and these two types of tests require a different approach to study ISE.

Sharp indentation tests (e.g., Berkovich tip) are only briefly discussed here because the present study is focused on spherical tips. It should be noted that using SGCP to model ISE with a sharp tip is more challenging than with the spherical tip as there are significantly greater stress and strain gradients. The lattice rotations for Berkovich tip were examined experimentally in series of papers by Rester et al. [35, 36, 37]. It was concluded that for the lowest loads the orientation changes are very small and dislocation sources are responsible on the hardness. At the highest loads, a fragmentation of misorientation patterns in the substructures was observed, which is responsible for the hardness decrease, the latter being a manifestation of ISE. The pile-up patterns and/or load-penetration curves, lattice rotation fields obtained from the simulations and experiments with Berkovich tip were compared in several works e.g. [38, 39, 40]. However, in the simulations the CP model without strain gradient enhancement was used, and the experiments were performed for one level of load, so the ISE was practically not considered. In experimental work by Wilkinson et al. [41], elastic strain, lattice rotations and GND distributions on the free surface around 500 nm deep Berkovich indents in coarse-grained Fe were determined. In [42, 43] the SGCP model was applied for Berkovich test, but the simulation results were limited to pile-up patterns or lattice rotations presented for one load level, and only the $P-h$ curves and/or hardness were compared with experimental data. A comprehensive study of ISE captured with Berkovich tip with the simulation of indentation test for different depths has not been found by the present authors.

An extensive study of ISE in wedge indentation (2D) was presented by Lewandowski and Stupkiewicz [44], using the ‘minimal’ gradient enhancement of CP by slip-rate gradients proposed in [45] and described below. The authors numerically determined the lattice rotations, load-penetration depth curves and GND densities for different penetration depths. All major features of the experimental response obtained without ISE in [46, 47] were very well reproduced, but no experimental data was found to compare ISE.

Generally, 3D FEM simulations of indentation tests using gradient-enhanced crystal-

plasticity as reviewed above are still scarce in the available literature. The above review shows also, that the sufficiency of existing CP models (with and without gradient enhancement) has not been sufficiently examined. Even if the agreement of experimental and theoretical results such as lattice rotation, pile-up patterns and GND densities was observed, it was achieved only at a certain load or for a certain tip radius and usually has a qualitative rather than a quantitative character. In particular, this is more evident for gradient-enhanced models.

Recently, it was shown [48, 49] that the size-dependence of hardness in spherical indentation tests on anisotropic Cu single crystals can be *predicted* by 3D finite element simulations using the ‘minimal’ gradient enhancement of crystal plasticity proposed by Petryk and Stupkiewicz [45], where an evolving length scale is fully determined through standard parameters of a non-gradient hardening law. This length scale, related to the slip-*rate* gradient effect on crystal hardening, differs substantially from that in the Nix-Gao model [5] and has a physical interpretation through its relation to the dislocation mean free path. The benefit of this approach was also used in this work.

This article presents a combined experimental and numerical study of size effects in indentation tests performed in a Cu single crystal with spherical indenters of various radii. Besides the usually observed increase in hardness with decreased size of the plastic zone, the deformed surface topography around the indent and lattice rotations beneath the indent are also investigated. Experimental techniques such as the atomic force microscopy (AFM), electron backscatter diffraction (EBSD) and transmission Kikuchi diffraction (TKD) were used to generate the results compared with numerical predictions obtained by the finite element method (FEM) using a model of gradient-enhanced crystal plasticity.

We follow the recent paper [49] where a relatively simple but effective numerical tool was proposed incorporating simultaneously two gradient-effects of (i) the gradient of the *accumulated* lattice rotation and (ii) the local incompatibility of the *rate* of plastic deformation. Effect (i) includes the Cosserat couple stresses and is responsible for kinematic hardening, and (ii) includes the enhancement of the hardening law by the PS-term responsible for extra isotropic hardening due to the local incompatibility of the rate of plastic deformation [45]. However, in distinction to that study we use here a power-hardening law that was fully calibrated using the stress-strain curve from the uniaxial compression test. The model is described below in Section 3, preceded by description in Section 2 of the experimental methods used. To verify the model, a number of quantities are compared with those measured directly in the experiment, i.e. load-penetration depth curves, nominal hardness, lattice rotations and surface pile-up/sink-in patterns (Section 4). The experiments were performed for a wide range of tip radii ($1.75 \div 250 \mu\text{m}$) and relatively large penetration depth ($h/R \approx 0.11$).

2. Experimental methods

In this section, sample preparation and selected parameters of micro- and nano-scale indentation tests are presented. The most important technical parameters of the test equipment are also specified. A complex procedure of sectioning samples for EBSD measurements is described. Some exemplary results are provided.

2.1. Nano- and micro-indentation

2.1.1. Spherical indentation tests

In the spherical indentation tests the (001)-oriented, high-purity (99.9999 %) copper single crystal samples were examined. The material was produced by MaTecK GmbH (Germany) using the Czochralski method. The samples ($10 \times 10 \times 5$ mm) were cut by wire saw, and then mechanically polished. The latter generates usually a thin hardened layer, which we removed by subsequent electro-polishing. Next, the samples were cleaned with distilled water and isopropyl alcohol and finally the polishing quality was checked by ultra-low force nanoindentation test. The procedure (electro-polishing and nanoindentation) was repeated until the residual penetration depth did not change in the subsequent steps, (Table 1). The effect of surface preparation can also be estimated by analysing indentation curves. The numerous pop-in events that occur during the tests (especially with spherical tips) and good repeatability, indicate a low defect density. After electro-polishing, R_a (roughness parameter) was equal to approximately 1 nm.

Table 1: Stages of electro-polishing.

residual penetration depth [nm] (for $R = 1.75 \mu\text{m}$, $P = 1.6 \text{ mN}$)	number of electro-polishing process
140	1
160	2
180	3
180	4

In the micro- and nano-indentation tests, the spherical tips with different radii were applied : $R = 1.75 \mu\text{m}$, $R = 50 \mu\text{m}$ (diamond), $R = 5.9 \mu\text{m}$, $R = 9.2 \mu\text{m}$, $R = 110 \mu\text{m}$ (sapphire), $R = 250 \mu\text{m}$ (tungsten carbide). The indentation tests were performed using the Anton Paar (previously CSM) MHT (micro) and UNHT (nano) testers (Open Platform equipment). At the micro-scale (tip radii $50 \mu\text{m}$, $110 \mu\text{m}$ and $250 \mu\text{m}$) the MHT micro-indenter, with the displacement resolution of 0.3 nm and load resolution of 100 μN , was used.

It is worth noting that the CSM/Anton Paar experimental device is equipped with an additional reference tip (or so-called reference fork for the micro-scale) that touches with small force the indented surface during the indentation. Therefore the indenter displacement is measured with respect to the non-deformed region of sample surface located far from the residual impression. This system considerably diminishes the frame compliance which can be attributed to the uncontrolled deflection of the indenter shaft rather than to the deflection of the specimen mount or the loading frame. The instrument exhibits also an extremely low thermal drift (0.0083 nm/s), which was practically negligible in our measurements. The frame compliance was calculated individually for each tip on the basis of the difference between the actual load-penetration depth ($P-h$) curve and the Hertz solution for spherical indentation in fused silica [50]. The calculated values were approximately 1.2-2.3 nm/mN and 0.04-0.07 nm/mN for nano- and micro-indentation, respectively. The load-controlled tests in quasi static regime were carried out. The duration of loading and unloading was 120 s and 60 s, respectively, with 2 s hold time. The assumed contact force was 0.005–0.01 mN at the nano-scale and 5 mN at the micro-scale.

To verify the repeatability of the tests, they were repeated several times, for each tip and level of load. The scatter of results was rather low, however, the different levels of

loads corresponding to the pop-in events were observed, and the number of the latter decreased with the increase of tip radius. This indicates that the examined single crystal is not perfectly homogeneous, that is, the density of existing dislocations may be different in different locations. The dependence of pop-in events on the presence of defects in single crystals has been analysed in numerous papers, e.g. [51], [52].

The examined single crystal was not completely homogeneous, which manifested itself through a different slope of the loading curves (after pop-in) at different indentation points (areas). We supposed that the somewhat greater slope of some P-h curves was due to higher strain-hardening and corresponded to a local higher density of pre-existing dislocations. In order to avoid the interplay of local differences in strain hardening and the size effect, a small number of P-h curves with distinctly higher slope have been neglected for each tip radius. Therefore, when investigating the size effect with different tips, we took into account the results obtained in regions with similar densities of pre-existing dislocations.

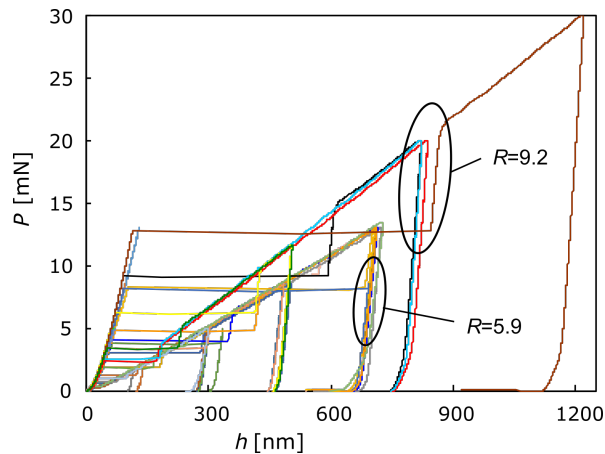


Figure 1: Exemplary result: Load-penetration depth curves for $R = 5.9 \mu\text{m}$ and $R = 9.2 \mu\text{m}$ tips (raw data from the indenter). After numerous pop-in events at different loads and at different locations, the curves return to the same slope for each tip.

2.1.2. Calibration of tip radii

The correct calibration of tip radius is a fundamental issue in the spherical indentation test. At the micro scale the radii of tips ($R = 50 \mu\text{m}$, $110 \mu\text{m}$ and $250 \mu\text{m}$) were measured directly with scanning profilometer that guarantees a sufficient accuracy. At the nano-scale, the indentation test in fused silica is usually applied to determine tip radius, however in this test the penetration depth is limited. Therefore, for greater penetration depths, we measured residual impressions in the investigated copper single crystal. The latter exhibits low elastic recovery (high elastic modulus to yield limit ratio), and one can assume that at large load the radius of the residual impression is very close to that of the tip. The details of calibration of the applied tips are presented in [22].

2.1.3. Friction coefficient

The friction coefficient was measured in reciprocating ball on disk test with sapphire ball with 6 mm diameter sliding on polycrystalline copper. The mean contact pressure at the beginning of friction, calculated with Hertz equation was 450 MPa. The test duration was approximately 180 s, since a steady state was established after this time, and the value of the friction coefficient was about 0.23. The effect of friction on indentation results is discussed in [53].

2.2. Measurements of residual impressions

At the micro scale, the 3D topography of residual impressions were measured with the Hommel-Etamic T8000 Nanoscan scanning profilometer, which has a vertical resolution less than 1 nm, and resolutions in X and Y direction are 0.1 μm and 0.5 μm , respectively. The radius of tip is equal 2 μm . The optical microscope was also used to capture the boundary of the smallest residual impressions. The atomic force microscope Nanit (Nanosurf, Swiss) integrated in the Anton Paar Open Platform device was used to measure residual impressions at the nano-scale. The maximum scan range (X, Y) is 110 μm , maximum Z-range 22 μm , and the resolution in Z direction (noise level) - 90 pm. On the basis of the acquired 3D maps, the profiles of residual impression in arbitrary direction can be generated.

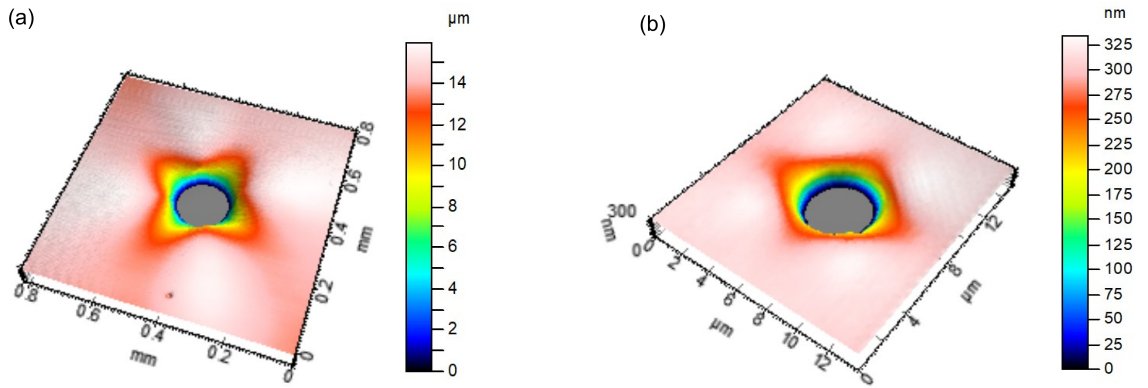


Figure 2: Exemplary residual imprints at micro and nano-scale: (a) tip radius $R = 250 \mu\text{m}$; (b) tip radius $R = 5.9 \mu\text{m}$. The bottoms of the imprints are cut-off, the 0-height starts at a half of the maximum penetration depth, to show pile-up patterns more clearly. At the micro-scale, the sink-in is more evident in the vicinity of the imprint and the dimensions of pile-ups are relatively larger (compared with the imprint dimension).

2.3. Preparation of cross-sections and misorientation measurements

The cross-sections through the center of indents for EBSD analysis were prepared in two steps. First, the wire saw with diamond suspension was used in order to initially cut the specimen in the safe vicinity of the indents (approximately 400 μm from their centres). Next, the ion milling/polishing system Hitachi IM4000 was used to remove the material without introducing any deformation up the centre of the indents. The exact position of the indents centre were previously marked using FIB. In the case of small indents, i.e. sphere radii 5.9 μm and 1.75 μm for which TKD technique was applied, the standard procedure of lamellae preparation using FIB thinning/polishing was used. The lamellae preparation was performed using Hitachi FB-2100 Scanning Ion Microscope. For both EBSD and TKD techniques the indentation direction as well as normal to the cross-section were parallel to the $\langle 100 \rangle$ type crystallographic direction (see Fig. 3).

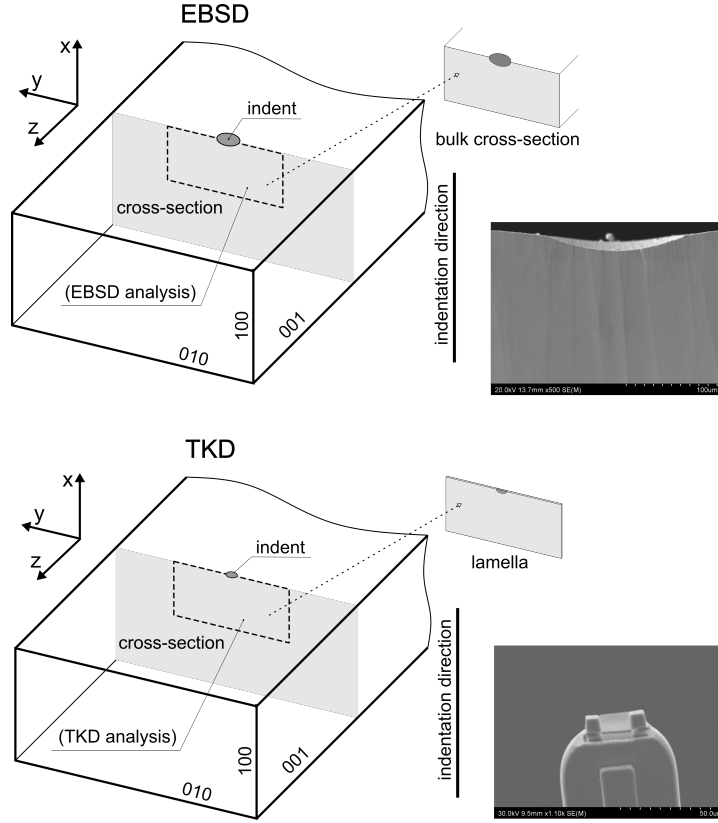


Figure 3: Scheme of cross-section for EBSD and TKD measurements. SEM images of bulk cross-section for $R = 250 \mu\text{m}$ and lamella for $R = 5.9 \mu\text{m}$ are shown.

The EBSD and TKD analyses were performed using Hitachi SU70 SEM with Oxford Instruments EBSD system. Depending on the indent radius a step of analysis was set from $1 \mu\text{m}$ to 10 nm . Main parameters used for both EBSD and TKD analyses are presented in Table 2. All obtained EBSD and TKD data was analysed using ATEX-software [54]. The GND density was calculated using the approach presented by Pantleon [55].

Table 2: EBSD and TKD parameters for all performed indentation tests.

indentation direction	sphere radius [μm]	technique	acceleration voltage [kV]	sample tilt [$^\circ$]	step [nm]
$\langle 100 \rangle$	250	EBSD	20	70	1000
$\langle 100 \rangle$	50	EBSD	20	70	200
$\langle 100 \rangle$	9.2	EBSD	20	70	100
$\langle 100 \rangle$	5.9	TKD	30	30	30
$\langle 100 \rangle$	1.75	TKD	30	30	10

2.4. Measurement of strain hardening in uniaxial compression

In order to determine the material parameters required for the numerical simulation of the indentation tests, the compression test was carried out for the examined copper single crystal. The samples with dimensions $5 \times 5 \times 10 \text{ mm}$ were cut by spark erosion. The Instron 5800 universal testing machine was applied in which the specimen fixturing was modified, i.e. the special compression platens, manufactured from hardened steel, dedicated to small samples were installed. The compression strain was measured by extensometer attached to the platens. The strain rate was equal to 0.0005 1/s .

3. Modelling

This section presents the assumptions and main features of the model used to simulate ISE. The micropolar elasto-plasticity approach to an anisotropic crystal is combined with the strain hardening law enhanced by an additional term that reflects the effect of the lattice spin gradient on the rate of isotropic hardening. The details of the applied finite element model are provided and a procedure for identification of material parameters is described.

3.1. Micropolar crystal elasto-plasticity

This part of the model presented in the small-strain format is well known; the reader is referred to papers by Forest et al. [56, 57] for more details.

As usual in the Cosserat continuum framework, we introduce the displacement \mathbf{u} and the micro-rotation field represented by the infinitesimal rotation vector $\boldsymbol{\phi}$. Based on these two independent kinematic fields two deformation measures are defined, i.e. the relative deformation tensor \mathbf{e} and the curvature tensor $\boldsymbol{\kappa}$

$$\mathbf{e} = \mathbf{H} + \boldsymbol{\epsilon} \cdot \boldsymbol{\phi}, \quad \boldsymbol{\kappa} = \text{grad } \boldsymbol{\phi}, \quad (1)$$

where $\mathbf{H} = \text{grad } \mathbf{u}$ denotes displacement gradient and $\boldsymbol{\epsilon}$ is the permutation tensor ($(\boldsymbol{\epsilon} \cdot \boldsymbol{\phi})_{ij} = \epsilon_{ijk} \phi_k$ in the index notation with the summation convention).

The stress tensor $\boldsymbol{\sigma}$ is associated with \mathbf{e} , and the couple-stress tensor \mathbf{m} is associated with $\boldsymbol{\kappa}$, both stress measures being non-symmetric in general. In the absence of body forces, they satisfy the balance equations

$$\text{div } \boldsymbol{\sigma} = \mathbf{0}, \quad \text{div } \mathbf{m} - \boldsymbol{\epsilon} : \boldsymbol{\sigma} = \mathbf{0}, \quad (2)$$

where the colon denotes a double contraction. Accordingly, we have $\sigma_{ij,j} = 0$ and $m_{ij,j} - \epsilon_{ijk} \sigma_{jk} = 0$. The boundary conditions are

$$\mathbf{t} = \boldsymbol{\sigma} \cdot \mathbf{n}, \quad \mathbf{M} = \mathbf{m} \cdot \mathbf{n}, \quad (3)$$

where \mathbf{n} is the outer unit normal to the domain boundary under consideration where the traction vector \mathbf{t} and couple-stress vector \mathbf{M} are prescribed.

Considering the small strain theory of an elastic-plastic Cosserat solid, the relative deformation measure \mathbf{e} is split additively into elastic (\square^e) and plastic (\square^p) parts. Assuming that the micro-rotation $\boldsymbol{\phi}$ contributes only to the elastic deformation one obtains the following relations

$$\mathbf{H} = \mathbf{H}^e + \mathbf{H}^p, \quad \mathbf{e} = \mathbf{e}^e + \mathbf{H}^p, \quad \mathbf{e}^e = \mathbf{H}^e + \boldsymbol{\epsilon} \cdot \boldsymbol{\phi}. \quad (4)$$

The displacement gradient and its constituents are further split into symmetric ($\boldsymbol{\epsilon}^\square = \mathbf{H}_{\text{sym}}^\square$) and skew-symmetric ($\boldsymbol{\omega}^\square = \mathbf{H}_{\text{skw}}^\square$) parts, so that we have

$$\mathbf{H} = \boldsymbol{\epsilon} + \boldsymbol{\omega}, \quad \mathbf{H}^e = \boldsymbol{\epsilon}^e + \boldsymbol{\omega}^e, \quad \mathbf{H}^p = \boldsymbol{\epsilon}^p + \boldsymbol{\omega}^p, \quad (5)$$

where $\mathbf{H}_{\text{sym}} = \frac{1}{2}(\mathbf{H} + \mathbf{H}^T)$, $\mathbf{H}_{\text{skw}} = \frac{1}{2}(\mathbf{H} - \mathbf{H}^T)$, etc.

The constitutive equations of the elastic response are adopted in the following form

$$\boldsymbol{\sigma} = \mathbb{L} : \mathbf{e}_{\text{sym}}^e + 2\mu_c \mathbf{e}_{\text{skw}}^e, \quad \mathbf{m} = 2\beta \boldsymbol{\kappa}, \quad (6)$$

which corresponds to three terms of the elastic strain energy,

$$W_e = \frac{1}{2} \mathbf{e}_{\text{sym}}^e : \mathbb{L} : \mathbf{e}_{\text{sym}}^e, \quad W_{\text{pen}} = \mu_c (\mathbf{e}_{\text{skw}}^e)^2, \quad W_\kappa = \beta \|\boldsymbol{\kappa}\|^2. \quad (7)$$

Here, \mathbb{L} is the fourth-order elastic stiffness tensor possessing the usual minor and major symmetries and describing classical elastic anisotropy. Two additional constants of Cosserat elasticity, μ_c and β , define the (isotropic) Cosserat part of the elastic response. Parameter β affects an intrinsic length scale of the micropolar continuum.

As in the conventional crystal plasticity, plastic distortion rate $\dot{\mathbf{H}}^{\text{P}}$ reads

$$\dot{\mathbf{H}}^{\text{P}} = \sum_{\alpha} \dot{\gamma}_{\alpha} \mathbf{N}_{\alpha}, \quad \mathbf{N}_{\alpha} = \mathbf{s}_{\alpha} \otimes \mathbf{m}_{\alpha}, \quad \mathbf{s}_{\alpha} \cdot \mathbf{m}_{\alpha} = 0 \quad (8)$$

where $\dot{\gamma}_{\alpha}$ is the shear rate on the slip system indexed by α , \mathbf{m}_{α} the slip-plane normal and \mathbf{s}_{α} the slip direction, \otimes denotes a tensor product, and $\mathbf{s}_{\alpha} \cdot \mathbf{m}_{\alpha} = 0$ is the condition of plastic incompressibility. The generalized resolved shear stress τ_{α} for the α -th slip system is defined as

$$\tau_{\alpha} = \boldsymbol{\sigma} : \mathbf{N}_{\alpha} = \tau_{\alpha}^{\text{sym}} - X_{\alpha}, \quad \tau_{\alpha}^{\text{sym}} = \boldsymbol{\sigma}_{\text{sym}} : (\mathbf{N}_{\alpha})_{\text{sym}}, \quad X_{\alpha} = -\boldsymbol{\sigma}_{\text{skw}} : (\mathbf{N}_{\alpha})_{\text{skw}}, \quad (9)$$

where $\tau_{\alpha}^{\text{sym}}$ is the classical resolved shear stress and X_{α} can be interpreted as a back stress. From Eq. (2)₂, we have $\boldsymbol{\sigma}_{\text{skw}} = \frac{1}{2} \boldsymbol{\epsilon} \cdot \text{div } \mathbf{m}$, and it follows that

$$X_{\alpha} = -\frac{1}{2} (\mathbf{s}_{\alpha} \times \mathbf{m}_{\alpha}) \cdot \text{div } \mathbf{m}, \quad (10)$$

where \times denotes a vector product. In the rate-independent plasticity, the slip system α is activated when the corresponding resolved shear stress τ_{α} reaches a threshold value, τ_{α}^c . In terms of the following yield functions f_{α} ,

$$f_{\alpha} = |\tau_{\alpha}| - \tau_{\alpha}^c = |\tau_{\alpha}^{\text{sym}} - X_{\alpha}| - \tau_{\alpha}^c, \quad (11)$$

the slip-system activity is governed by

$$f_{\alpha} \leq 0, \quad (\text{sign } \tau_{\alpha}) \dot{\gamma}_{\alpha} \geq 0, \quad f_{\alpha} \dot{\gamma}_{\alpha} = 0. \quad (12)$$

In the finite-element implementation below, a viscous regularization of conditions (12) is used, see Section 3.4.

Lattice rotation $\boldsymbol{\omega}^e = \boldsymbol{\omega} - \boldsymbol{\omega}^{\text{P}}$ is defined as the difference between the material rotation $\boldsymbol{\omega}$ and the plastic rotation $\boldsymbol{\omega}^{\text{P}} = \mathbf{H}_{\text{skw}}^{\text{P}}$. From Eq. (4)₃, we have

$$\boldsymbol{\omega}^e = \mathbf{e}_{\text{skw}}^e - \boldsymbol{\epsilon} \cdot \boldsymbol{\phi}. \quad (13)$$

When the penalty parameter μ_c is sufficiently large, $\mathbf{e}_{\text{skw}}^e$ must be small, and $\boldsymbol{\omega}^e$ becomes close to the Cosserat micro-rotation,

$$\boldsymbol{\omega}^e \approx -\boldsymbol{\epsilon} \cdot \boldsymbol{\phi}. \quad (14)$$

The well-known dislocation density tensor $\boldsymbol{\alpha}$ is introduced as a measure of the incompatibility of plastic or elastic deformation [58],

$$\boldsymbol{\alpha} = \text{curl } \mathbf{H}^{\text{P}} = -\text{curl } \mathbf{H}^e = -\text{curl } \boldsymbol{\epsilon}^e - \text{curl } \boldsymbol{\omega}^e, \quad (\text{curl } \boldsymbol{\omega}^e)_{ij} = \epsilon_{jkl} \frac{\partial (\boldsymbol{\omega}^e)_{il}}{\partial x_k}. \quad (15)$$

Neglecting the curl of elastic strain, $\text{curl } \boldsymbol{\varepsilon}^e \approx \mathbf{0}$, and substituting Eq. (14), the dislocation density tensor is finally approximated by

$$\boldsymbol{\alpha} \approx \text{curl}(\boldsymbol{\varepsilon} \cdot \boldsymbol{\phi}) = \boldsymbol{\kappa}^T - (\text{tr } \boldsymbol{\kappa})\mathbf{1}, \quad (16)$$

where the last equality follows from the identity: $\text{curl}(\boldsymbol{\varepsilon} \cdot \boldsymbol{\phi}) = (\text{grad } \boldsymbol{\phi})^T - (\text{div } \boldsymbol{\phi})\mathbf{1}$. The right-hand expression (16) is known as the Nye tensor [59], where tensor $\boldsymbol{\kappa}$ is interpreted as the lattice curvature in view of approximation (14). As shown in [49], this expression is suitable for finite-element implementation within the Cosserat continuum framework and, in particular, can be used to effectively implement the gradient-enhanced hardening law that is discussed in the subsequent section.

3.2. Gradient-enhanced incremental hardening

A simple proposal by Petryk and Stupkiewicz [45] to include the *incremental* incompatibility of plastic flow in the hardening rule has been used and described in several recent papers, therefore only a brief account is given here. The idea was to enhance the conventional anisotropic incremental hardening law for a single crystal, expressed in terms of the slip rates on crystallographic systems, by an extra term dependent on the *gradients* of current slip rates, viz.

$$\dot{\tau}_\alpha^c = \theta \sum_\beta q_{\alpha\beta} |\dot{\gamma}_\beta| + \underbrace{\theta \ell \dot{\chi}}_{\text{PS term}}, \quad \theta \ell = \frac{a^2 \mu^2 b}{2\tau^c}. \quad (17)$$

In the derivation, the conventional state-dependent hardening moduli $h_{\alpha\beta}$ that specify self ($\alpha = \beta$) and latent ($\alpha \neq \beta$) hardening are expressed as $h_{\alpha\beta} = \theta q_{\alpha\beta}$, with θ as an isotropic hardening modulus. The Taylor formula [60] for the relationship between the isotropic flow stress τ^c and the total dislocation density ρ was used to derive the PS term,

$$\tau^c = a\mu b\sqrt{\rho}, \quad (18)$$

where coefficient a is a given material constant, μ the elastic shear modulus, and b the Burgers vector modulus. Formula (18) is adopted regardless of the *accumulated* incompatibility of plastic deformation measured by the dislocation density tensor $\boldsymbol{\alpha}$. As the next key step, it has been postulated that *not* ρ *itself*, but rather its *rate* $\dot{\rho}$ is decomposed into the sum of two scalar density *rates* of statistically and geometrically induced dislocations. The former obeys the usual multiplication/annihilation law [61] as in the absence of geometrically induced dislocations, and the latter denoted by $(\dot{\rho})_G$ is related to the rate of $\boldsymbol{\alpha}$ through

$$(\dot{\rho})_G = \frac{1}{b} \dot{\chi}, \quad \dot{\chi} = \|\dot{\boldsymbol{\alpha}}\|, \quad (19)$$

where $\dot{\chi}$ is the *effective slip-rate gradient*, and $\|\dot{\boldsymbol{\alpha}}\| = \sqrt{\dot{\boldsymbol{\alpha}} : \dot{\boldsymbol{\alpha}}}$.

From formula (16) we obtain [49]

$$\dot{\chi} \approx \sqrt{\dot{\boldsymbol{\kappa}} : \dot{\boldsymbol{\kappa}} + (\text{tr } \dot{\boldsymbol{\kappa}})^2}. \quad (20)$$

Importantly, the coefficient $\theta \ell$ at $\dot{\chi}$ in Eq. (17) and the internal length scale ℓ are expressed solely in terms of standard quantities of a non-gradient hardening law. Therefore, no additional assumption is needed to specify the PS term and thus calculate the effect of current slip-rate gradients on crystal hardening. Moreover, the internal length scale ℓ

has a physical interpretation through its relation to the dislocation mean free path λ , and simply amounts to $\ell = \lambda$ in the absence of dislocation annihilation [45]. From Eq. (17)₂ it follows that ℓ is not a constant parameter but evolves during the deformation process as a given function of τ^c and θ . Note a substantial difference between ℓ above and the characteristic length scale in the Nix-Gao model [5]; both are derived using the Taylor formula (18) but on different routes and in effect are different quantities [45].

3.3. Finite element modelling of spherical indentation test

The implementation of the balance equations in their respective weak forms was similar to that in [49] and carried out in a displacement-based finite element code. In total, the formulation requires six degrees of freedom per node, i.e. three displacement and three micro-rotations. A locking-free hexahedral eight-node element, similar to the one proposed by Korelc [62], is used in the present work, where both fields are interpolated with trilinear shape functions. The resulting coupled finite-element equations were solved monolithically by employing the Newton method.

The implementation and simulation were performed via AceGen/AceFEM packages which, together with the symbolic capabilities of *Mathematica* [63], provide tools for convenient numerical implementation and for solving computational tasks [64].

The standard Coulomb friction model is used in the frictional contact problem in 3D indentation, where the indenter is modelled as a rigid sphere and the impenetrability constraints are enforced using the augmented Lagrangian method. Importantly, it is assumed that the couple stress vector \mathbf{M} in boundary condition (3) vanishes on the entire free surface, and no additional non-standard contact conditions are imposed.

In this study, numerical simulations were conducted to investigate size effects in the spherical indentation in a (001)-oriented, high-purity copper (fcc) single crystal. The simulations were performed for various indenter radii, and the finite element mesh used in the simulations is displayed in Fig. 4. To exploit the crystal symmetry, the computational domain was reduced to one quarter with additional constraints on the xy and xz planes. The normal displacement and ϕ_x and ϕ_y micro-rotations were blocked on the xy plane, while the normal displacement and ϕ_x and ϕ_z micro-rotations were blocked on the xz plane. The total length of the cube side is scaled with the nominal contact radius and it is set to be $16.8a_{\max}$ where $a_{\max} = \sqrt{h_{\max}(2R - h_{\max})}$. The maximum penetration depth h_{\max} scales with the indenter radius R and it is set to be $h_{\max}/R = 0.12$. Simulations for all radii were performed for a constant velocity $v = h_{\max}/t_{\max}$ with $t_{\max} = 100$ s.

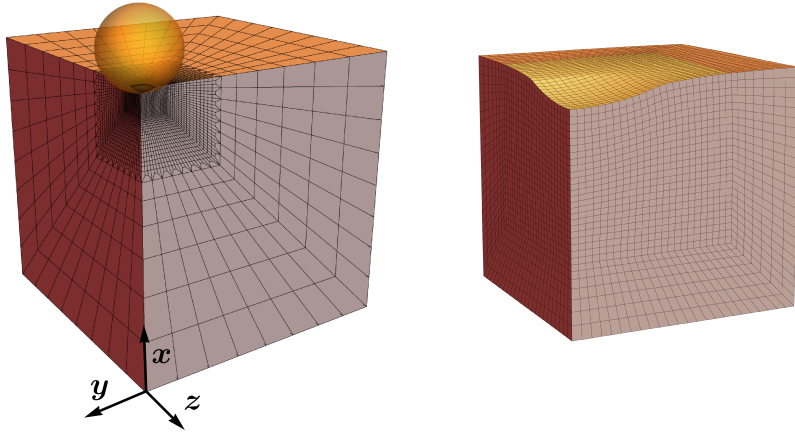


Figure 4: Finite element mesh of the computational domain (left) and an enlarged detail of the mesh showing the deformation pattern beneath the indenter (right).

3.4. Identification of material parameters

Most of the parameters for high purity Cu single crystal involved in the proposed model are standard and can be found in the existing literature, e.g., standard elastic constants $c_{11} = 170$ GPa, $c_{12} = 124$ GPa, $c_{44} = 75$ GPa for a Cu cubic crystal are taken after [65, 66]. Parameters that appear in the Taylor formula can be specified based on the paper [67], i.e. the strengthening coefficient $a = 0.33$, the Burgers vector modulus $b = 0.256$ nm for Cu, and the shear modulus μ is calculated as the one for $\{111\}\langle 110\rangle$ slip systems, i.e. $\mu = (c_{11} - c_{12} + c_{44})/3 = 40.3$ GPa. The initial yield stress for pure copper, equal for all slip systems, is taken as $\tau_0 = 1$ MPa, cf. [65, 61].

A three-parameter power hardening law is used which was shown [28] to be useful in identifying the hardening exponent from pile-up and sink-in profiles without taking gradient effects into account, i.e.

$$\tau_{\Gamma}^c = C(\Gamma_0 + \Gamma)^n, \quad \dot{\Gamma} = \sum_{\alpha} |\dot{\gamma}_{\alpha}|. \quad (21)$$

The gradient-enhanced hardening law (17) is simplified in the following way: $q_{\alpha\beta} = 1$, $\theta = d\tau_{\Gamma}^c/d\Gamma$ and $\dot{\tau}_{\alpha}^c = \dot{\tau}^c = \dot{\tau}_{\Gamma}^c + \theta\ell\|\dot{\boldsymbol{\alpha}}\|$. This extreme simplification has not been tested before in the context of ISE.

Three parameters which appear in the above equation, related to material behaviour in the plastic regime, $\Gamma_0 = 0.00035$, $C = 119$ MPa and $n = 0.6$ have been identified from the [001] uniaxial compression curve (Fig. 5) and verified with indentation test for $R = 250$ μm (Fig. 6), hence in the cases where no gradient effects are expected. The parameters are coupled by the choice of a reference value of Γ for which the graphs described by Eq. 21 for various n cross each other at a single point [28]. Then, as shown in Fig. 6(a), the parameter n practically does not affect the load-penetration depth curve and can be verified by fitting to the experimental surface pile-up and sink-in profiles. In Fig. 5 it is shown that $n = 0.5 \div 0.6$ corresponds to satisfactory agreement in the case of uniaxial compression test. In effect, the strain hardening law was fully calibrated using the stress-strain curve from the uniaxial compression test, while pile-up and sink-in profiles from the spherical indentation test for $R = 250$ μm were only used to confirm the choice $n = 0.6$.

The Cosserat formulation involves two other, rather non-standard parameters μ_c and β . According to Eqs. (7)₂ and (13), μ_c is treated as a penalty parameter and hence must

be high enough so that the micro-rotation field ϕ be close to the lattice rotation, and is taken as $\mu_c = 10 \mu = 403$ GPa, which was found to satisfy the above requirement (cf. [49]).

Parameter β plays here two roles, on one hand it provides required regularization, as explained in detail in [49], and on the other hand it plays an important role in the modelling of the misorientation angle field as it is discussed in this paper. It was found that $\beta = 0.03$ GPa μm^2 gives reasonable values of the misorientation angle for $R = 1.75$ μm and at the same time does not disturb too much the macroscopic effect of the PS term (cf. Sec. 4.4).

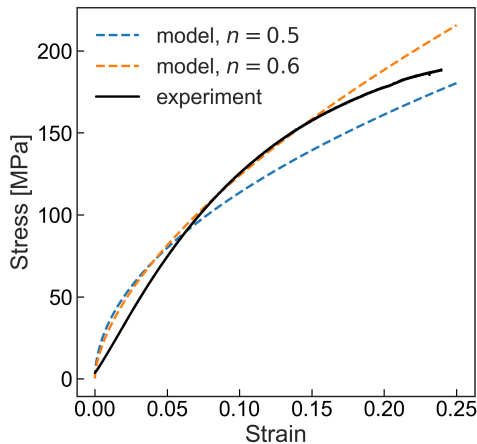


Figure 5: Comparison of the experimental (solid line) true stress vs true strain curve for compression in [001] direction of a pure Cu single crystal with the model. The calculated dashed lines intersect at a prescribed strain 0.4 and show the numerical results described by the power hardening law (21) for two values of exponent n .

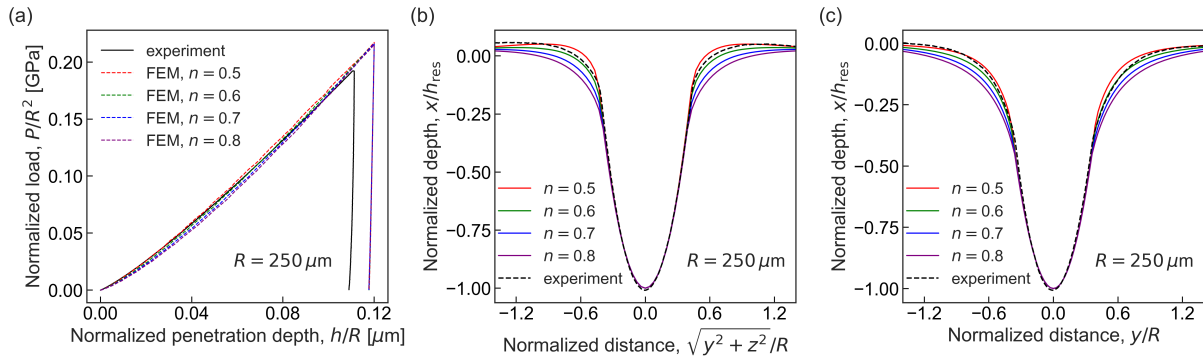


Figure 6: The influence of hardening exponent n on (a) the load-penetration depth curve, (b) surface pile-up profiles (along radial direction $y = z$ in Fig. 4), and (c) surface sink-in profile (along radial direction $z = 0$ in Fig. 4) upon unloading, for $R = 250$ μm and the residual penetration depth $h_{\text{res}} \approx 0.11R$. Comparison of the experimental and numerical results allows for a satisfactory verification of the choice of $n = 0.6$.

The well-known problem of non-uniqueness in the selection of active slip systems is circumvented here in a rather common way by employing a rate-dependent version of the crystal plasticity model, which results in the following explicit equation for the plastic slip rate on each slip system [68],

$$\dot{\gamma}_\alpha = \dot{\gamma}_0 \text{sign}(\tau_\alpha) \left(\frac{|\tau_\alpha|}{\tau_\alpha^c} \right)^m. \quad (22)$$

In order to ensure that the computational results are close to the rate-independent response, the two additional parameters which characterize rate sensitivity are set to $\dot{\gamma}_0 = 0.001 \text{ s}^{-1}$ and $m = 50$.

The material parameters used in numerical simulations are summarized in Table 3.

Table 3: Material parameters for a Cu single crystal used in numerical simulations.

c_{11}	c_{12}	c_{44}	τ_0	Γ_0	C	n	$\dot{\gamma}_0$	m	a	μ	b	μ_c	β
[GPa]	[GPa]	[GPa]	[MPa]	[-]	[MPa]	[-]	[s^{-1}]	[-]	[-]	[GPa]	[nm]	[GPa]	[GPa μm^2]
170	124	75	1	0.00035	119	0.6	0.001	50	0.33	40.3	0.256	403	0.03

4. Results and discussion

In this section, the experimental and simulation results are presented and compared in order to verify the effectiveness of the proposed model. Variables measured in the tests performed, such as P-h curves, lattice misorientation distributions, and surface pile-up and sink-in profiles, are compared with those from the modelling. The results are discussed along with the effect of changes in selected model parameters on the simulation results.

4.1. P-h curves – experimental and modelling

The load-penetration depth curves presented in this study, extracted from unpublished raw data associated with a prior publication [22], offer valuable insight into the size-dependent material response during spherical indentation. For each tip radius, several curves have been selected that are closest to the average plot for that tip. In Fig. 7 a comparison is made between the experimental curves and the numerical results obtained using the Cosserat crystal plasticity model incorporating the PS term. The numerical results, represented by the black dashed lines, align remarkably well with the experimental data beyond the stage of pop-in events as illustrated by the coloured solid lines.

It is worth emphasizing that the computational results for all indenter radii were obtained using the same set of parameters calibrated without taking into account increasing strain gradients. Hence, the level of agreement between the experimental and computational results in Fig. 7 may be regarded as highly satisfactory. This confirms the robustness of the present crystal plasticity model and its ability to accurately *predict* macroscopic behaviour in indentation tests. Clearly, the model is unable to describe experimentally observed pop-in events.

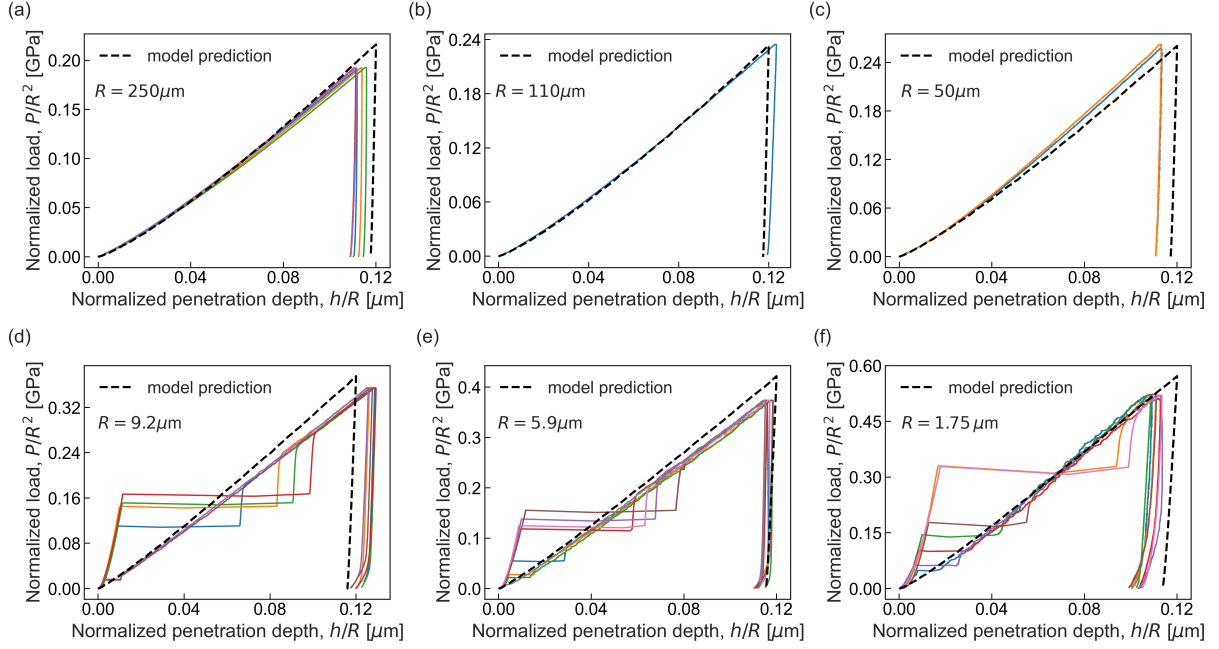


Figure 7: Load-penetration depth curves measured (solid lines) and calculated (dashed lines) for spherical indentation in copper single crystal in [001] direction with different tip radii. The clearly different response shown in Figs. (a)-(f) indicates significant size effects that are correctly predicted by the model in numerical simulations, despite transient stochastic pop-in events not covered by the deterministic model.

4.2. Misorientation of the crystallographic lattice – experimental

In Fig. 8 the maps of misorientation angle with respect to initial orientation of the crystals (Euler angles (0,0,0)) for all considered sphere radii R after indentation up to residual depth $h_{\text{res}}/R = 0.11 \pm 0.01$ are presented. It can be seen that both the distributions of misorientation angle and their maximal values change when the indenter radius changes. For the largest sphere radius, directly beneath the imprint, a triangular-shaped area with a clearly defined low-angle boundary (maximal misorientation angle of approximately 4 degrees) can be observed. This area becomes increasingly difficult to identify as the radius decreases. It is also evident that maximal misorientation angle decreases as the indenter radius decreases. The maximal values of the misorientation angle change from approximately 23 degrees for indenter radius 250 μm to about 2.5 degrees for 1.75 μm indenter radius. For all considered radii the maximal values are observed in the vicinity of the edge of the indents. In the same figure the rotations around x , y and z axes are shown. The rotation around normal to the cross-section is dominant for all considered indenter radii. Slightly asymmetric distribution observed for 9.2 μm radius can be a result of indentation of not perfectly flat surface in this particular case.

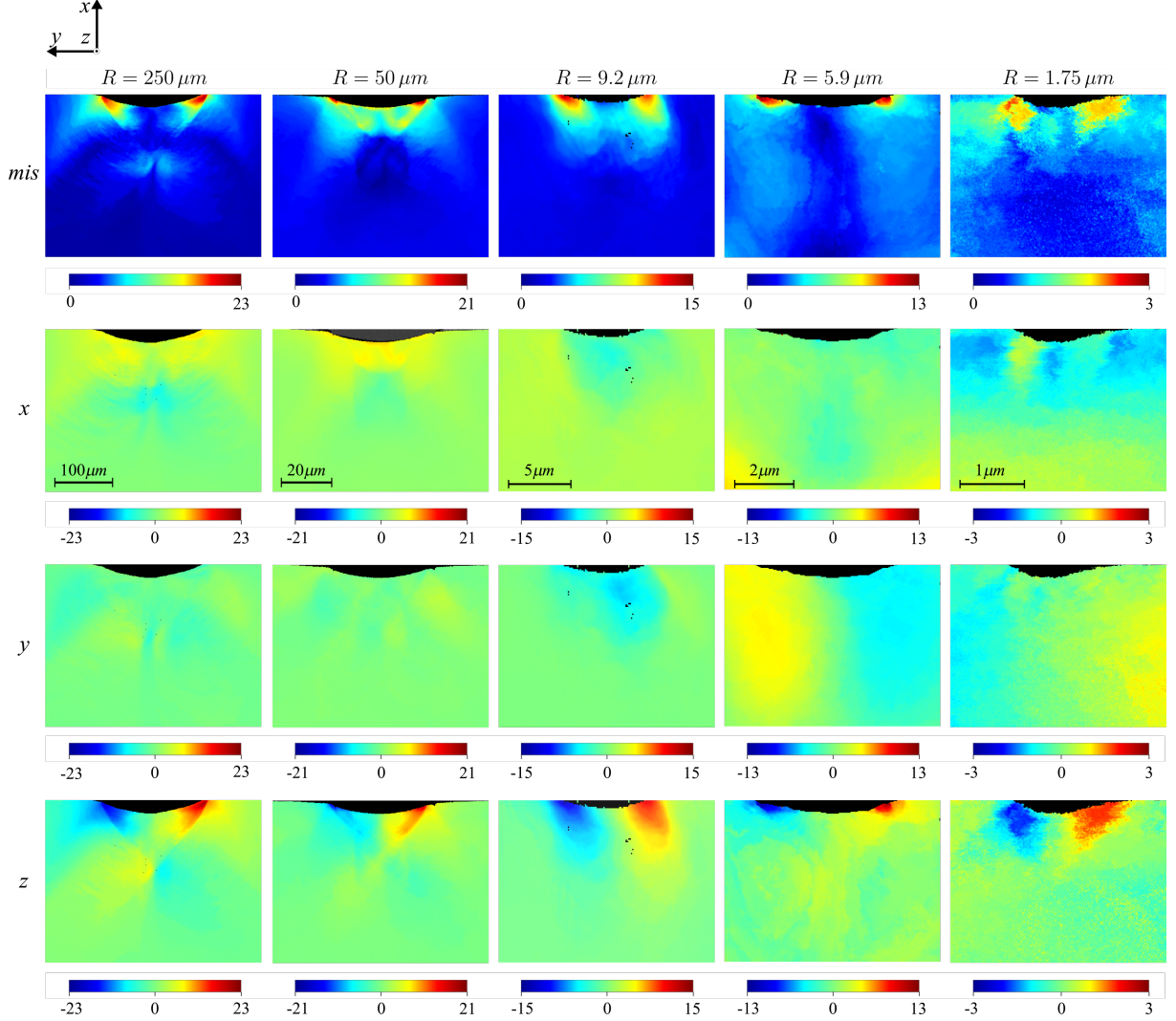


Figure 8: Comparison of misorientation angle distributions and the rotations around x , y and z axes after indentation to residual depth $h_{\text{res}}/R = 0.11 \pm 0.01$ for sphere radii R from $250 \mu\text{m}$ to $1.75 \mu\text{m}$.

For each sample cross-section analysed with EBSD (Fig. 8), a region was selected in the form of a narrow rectangle whose length l was much larger than its width s . The rectangles started in an area where the maximum misorientations occur, and their positions and the l/R and s/R ratios were the same for all the tip radii used. The exemplary rectangle marked on the misorientation map corresponding to $R = 250 \mu\text{m}$ is shown in the insert in Fig. 9. For each EBSD map (i.e. for each tip radius), the mean norm of the Nye tensor (16) in the selected rectangle was determined. For this purpose, the norm of the Nye tensor at the points within the rectangle was calculated using ATEX software [54] on the basis of the previously measured misorientation maps. The mean value was calculated taking into account all points in the selected area.

Fig. 9 shows the changes of the square root of the mean norm of the Nye tensor determined as above and of the nominal hardness with respect to the tip radius. The indentation size effect is manifested by the increase in hardness when the tip radius decreases. It is observed that the increase of the root of the mean norm of the Nye tensor with decreasing tip radius is qualitatively similar to the change of hardness. This can be explained by referring to the Taylor's formula (18), where the flow stress related to hardness is proportional to the square root of the total dislocation density, whose growth

is incrementally affected, according to Eq. (19), by the norm of the Nye tensor increment.

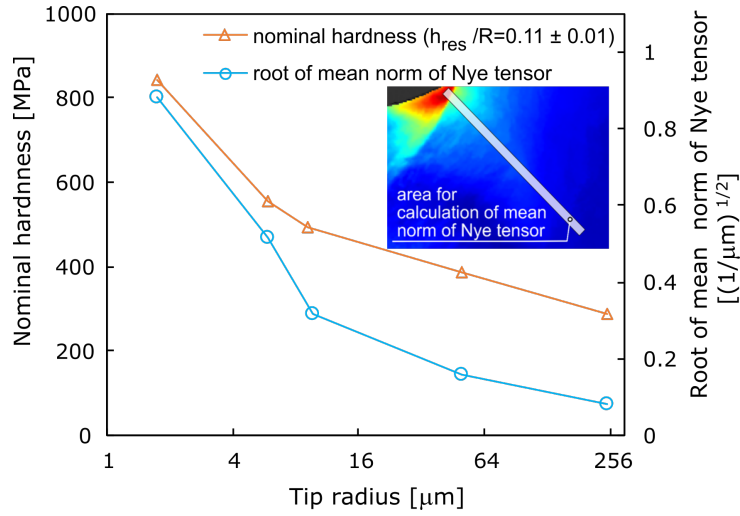


Figure 9: Observed nominal hardness and the root of mean norm of the Nye tensor (in the area selected on the misorientation map) as a function of tip radius.

4.3. Misorientation of the crystallographic lattice – modelling

In the modelling of size effects in spherical indentation, lattice rotations play a key role, especially due to their association with lattice curvature and GNDs. As the indenter penetrates the material, the significance of non-uniform lattice rotations during deformation becomes clear as they directly affect the generation, density, and distribution of GNDs in the crystal structure. In turn, the appearance of GNDs, which increases the total dislocation density, significantly influences the mechanical response of the material at the microscale. Accurate representation of lattice rotations in models is therefore essential to capture the intricate relationship between size effects and the emergence of GNDs, enabling a more realistic simulation of the anisotropic nature of deformation.

In the two figures below (Figs. 10 and 11), numerical results of the misorientation angle distribution are shown for different indenter radii. These pictures can be directly compared to the first and the last row of the experimental results, respectively, presented in Fig. 8. It is shown that maximal values as well as distributions change with the value of the indenter radius. For higher values of the indenter radius (e.g. $R = 250 \mu\text{m}$ or $R = 110 \mu\text{m}$, Figs. 10(a) and 10(b)), distributions of the maximum values of rotations are concentrated near the surface and the maximum values reach 16° . For smaller radii, however, the maximum values drop to about 6° for the smallest radius, the distribution is more smoothed out into lower parts of the body (Fig. 10(e)). The above described features agree at least qualitatively with the experimental data above. It should be emphasized that such effect of decreasing maximum values of rotation angles with decreasing indenter radii was achieved by adjusting parameter β related to the Cosserat curvature energy (see discussion in Section 4.4).

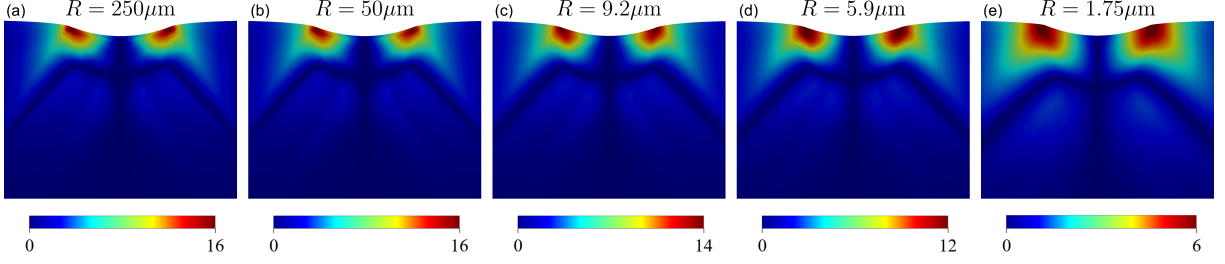


Figure 10: Misorientation angle in $[\circ]$ for different indenter radii $R = 1.75 - 250 \mu\text{m}$. A significant drop of misorientation angle with decreasing indenter radius R was obtained by adjusting parameter β related to the curvature energy.

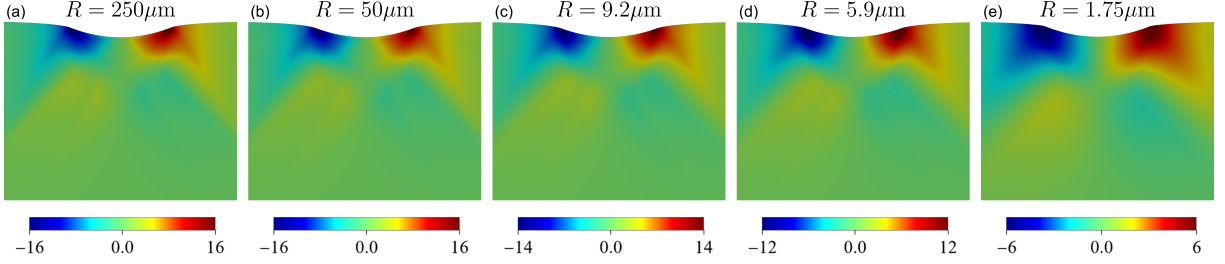


Figure 11: Rotation, ϕ_z in $[\circ]$, around z axis for different indenter radii $R = 1.75 \div 250 \mu\text{m}$. As in Fig. 10, a significant decrease in the rotation angle with decreasing indenter radius R was obtained by adjusting parameter β related to the curvature energy.

Given that the emergence of GNDs is recognized as a crucial factor contributing to size effects, accurately predicting their configuration is important. Accumulation of GNDs is intricately linked to the local misorientation of crystal lattice planes, accommodating the gradient of plastic deformation and serving as its valuable indicator.

Figure 12 shows, for various indenter radii, the distribution of the norm of the Nye tensor, (Eq. (16)), closely linked to the gradient of lattice rotation and usually interpreted as GND density. Remarkably, as depicted in the figure, the maximal density of GNDs increases with decreasing indenter radius, aligning with the expected behaviour. However, the increase in the maximal $\|\alpha\|$ is slower than in the reciprocal of the indenter radius R . This intriguing relationship suggests that the influence of the indenter size on the distribution of GNDs is more nuanced than a straightforward inverse proportionality. Understanding the interplay between indenter size and GND distribution, as revealed in Fig. 12, offers valuable insight into the microscale plastic deformation mechanisms during spherical indentation.

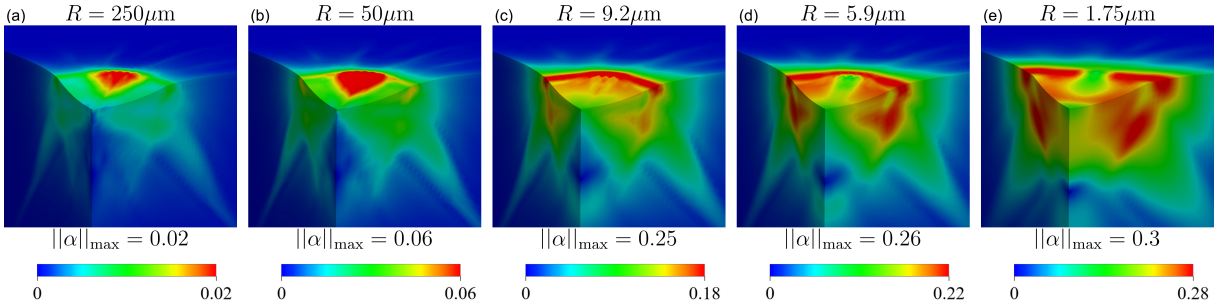


Figure 12: The norm of the Nye tensor, $\|\alpha\|$ in $1/\mu\text{m}$, as the measure of GND density, for different indenter radii $R = 1.75 - 250 \mu\text{m}$. As expected, the maximum GND densities are much higher for smaller indenter radii.

4.4. The effect of the coefficient β of lattice curvature energy

In the previous paper [49], it has been shown that the PS term has a crucial influence on modelling the size effect on hardness in the spherical indentation test, while the Cosserat model itself, without the PS term involved, is insufficient to predict the macroscopic size-dependent response correctly. The Cosserat framework was used there as the regularization tool, and the parameter β was chosen such that not to disrupt the macroscopic response in a significant way. The value $\beta = 0.0025 \text{ GPa } \mu\text{m}$ was found to be sufficient to provide required regularization. However, for that value of β the numerical results showed rather weak size-dependence of the micro-rotation field. In this section it is shown that the adjusted lattice curvature energy through manipulating the parameter β can be helpful in modelling size-dependent microstructural features, such as the misorientation angle.

Fig. 13(a) shows the influence of parameter β on the macroscopic load-penetration response for tip radius $R = 1.75 \mu\text{m}$. For small values of β the numerical response slightly overestimates the load for other material parameters as listed in Table 3. With increasing β , the curvature κ decreases (so does its rate $\dot{\kappa}$) because it is penalized by the corresponding elastic energy, which results in the smaller macroscopic size effects (cf. [49], Sec. 6.2). β parameter affects also pile-up and sink-in profiles, as shown in Figs. 13(b) and 13(c). It can be seen that for higher values of β the pile-ups and sink-ins are slightly smaller. However, this effect is not sufficient, given the current form of curvature energy for constant β , for obtaining good agreement with experimental results for tip radius $R = 1.75 \mu\text{m}$.

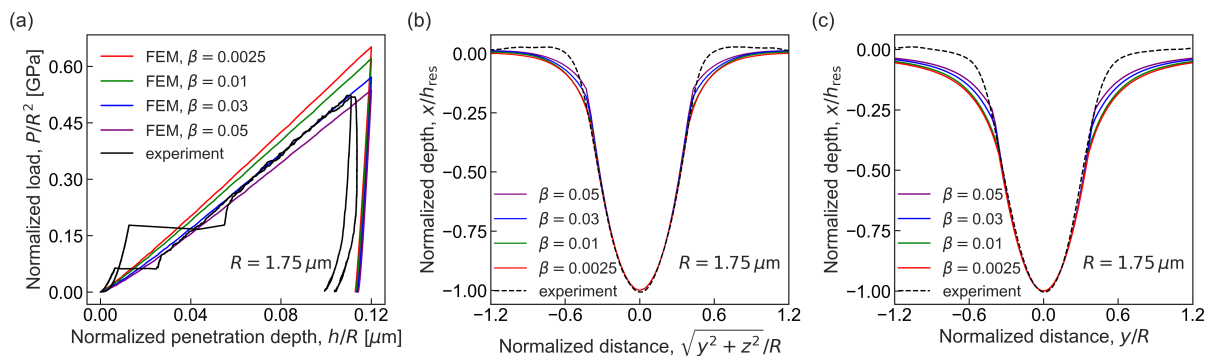


Figure 13: The influence of β parameter on (a) the load-penetration depth curve, (b) surface pile-up profiles, and (c) sink-in profiles, for $R = 1.75 \mu\text{m}$. A higher β results in (a) lower loads for the same penetration depth and a somewhat smaller discrepancy between experiment and simulation for (b) the surface pile-up profile (along $y = z$ radial direction in Fig. 4) and (c) surface sink-in profile (along $z = 0$ radial direction in Fig. 4).

The original input of the present modelling is that the appropriate fit of the β parameter results in a much better prediction of the maximal values and distributions of the misorientation angle at small scales. In Fig. 14 the misorientation angle distributions are shown for several values of parameter β . It is shown that for a small value of $\beta = 0.0025 \text{ GPa } \mu\text{m}^2$ the maximum value of misorientation is about 13° (Fig. 14(a)) and less only by 3° in comparison to that for the largest indenter radius $R = 250 \mu\text{m}$, and the distribution is also similar. On the other hand, for the highest considered value of $\beta = 0.05$ the maximum value of misorientation angle reaches about 4° (Fig. 14(d)), which is close to the experimental value reported above. Moreover, the distribution is less concentrated near the surface and spreads to the lower parts of the body, which is similar to

the experimental results for small indenter radius.

In Fig. 15, the GND's distributions, whose measure is defined as the norm of the Nye tensor, are shown for various values of β parameter. Since the Nye tensor depends on the gradient of micro-rotation field, its penalization is higher if β is increased. Hence, the GND's distribution is less concentrated near the indenter boundary and it is smoothed out within the crystal. It corresponds also to lower maximum values of the misorientation angle itself (Fig. 14).

The β effect can be easily explained: If β is increased for given R , the curvature κ (and hence the gradient of the micro-rotation field) is reduced since it is penalized by the related elastic curvature energy. Such curvature limitation by increasing β parameter, which results in smaller maximal values of GND density, may thus have physical interpretation.

In the light of other reports where the authors claim that GND's alone cannot explain size effects fully, the most important conclusion from our studies in this section is that substantial reduction of misorientation angle can be obtained by increasing the value of parameter β (Fig. 14). This reduction corresponds to much lower maximal values of the GND density measure for higher β (Fig. 15). Nevertheless, a significant dependence of GND density magnitude on indenter radius R is also observed for higher β , so that macroscopic size effects as in Fig. 7 can still be predicted with good accuracy. It is rather clear that the GND density distribution, misorientation field and sink-in/pile-up profiles are mutually correlated.

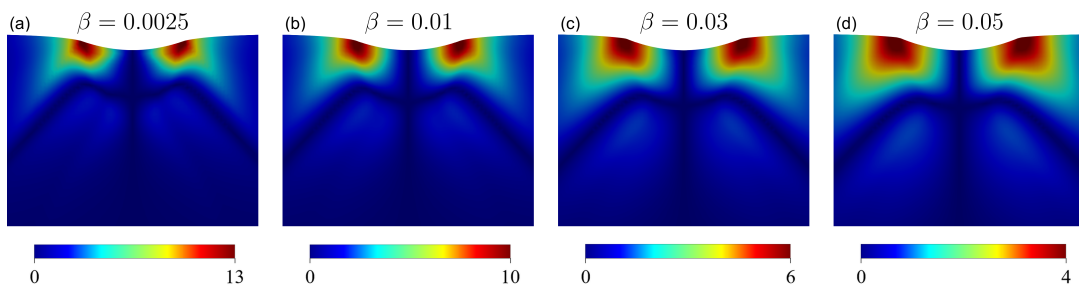


Figure 14: Distributions of misorientation angle, ϕ_{mis} [$^{\circ}$], for different values of parameter β [$\text{GPa } \mu\text{m}^2$] for $R = 1.75 \mu\text{m}$. For higher β the maximal value of misorientation angle is substantially decreased.

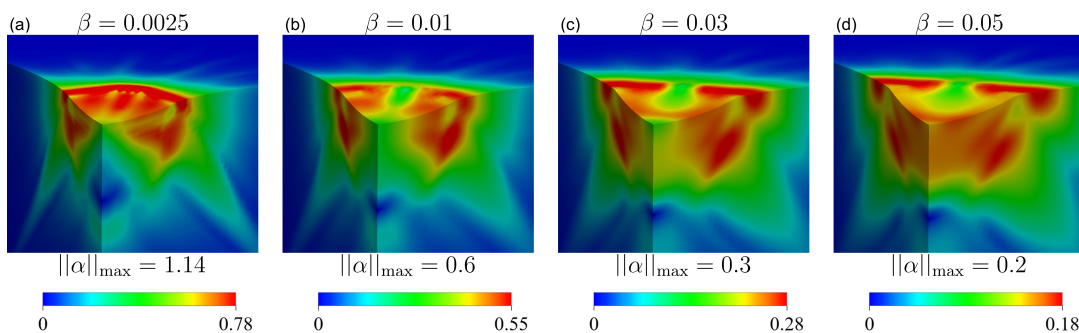


Figure 15: The norm of the Nye tensor, $\|\alpha\|$ in $1/\mu\text{m}$, for different values of parameter β for $R = 1.75 \mu\text{m}$. With increasing parameter β the maximal values of GND's are getting smaller, which corresponds to different GND density distributions and better predictions of the misorientation angle.

4.5. Discussion

As shown in Section 4.1, the agreement between the computational and experimental load-penetration depth curves beyond the stage of pop-in events may be regarded as highly

satisfactory. The agreement is even more striking when comparing the size effect on the resulting nominal hardness, as shown in Fig. 16. This confirms the previous conclusion [48, 49] that the PS term [45] in the hardening law (17) is itself sufficient to *predict* the size-effect on the indentation load accurately, without the use of any fitting parameter. This conclusion has been found insensitive to other features of the hardening law like the specific parametrization of the stress-strain curve in uniaxial compression.

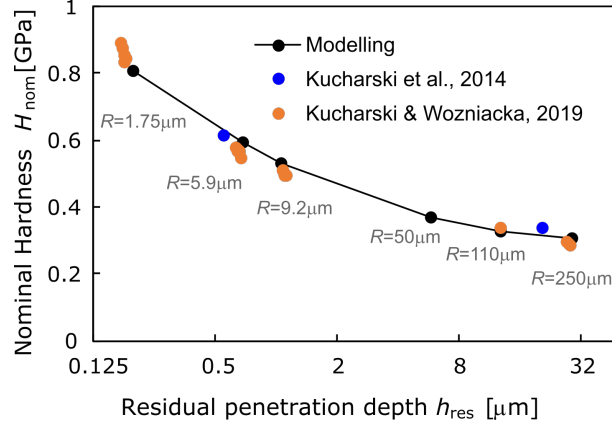


Figure 16: Dependence of the nominal hardness, $H_{\text{nom}} = P_{\text{max}}/A_{\text{nom}}$, where $A_{\text{nom}} = \pi h_{\text{res}}(2R - h_{\text{res}})$, on the residual penetration depth for the ratio $h_{\text{res}}/R \approx 0.11$.

There is still certain discrepancy in the shape of the residual imprint predicted by model and measured in the experiment. A satisfactory agreement between the experimental pile-up and sink-in profiles with the results of simulations has been reached for the power-hardening law with exponent $n = 0.6$ for a large tip radius $R = 250 \mu\text{m}$, as shown in Fig. 17 extracted from Fig. 6. However, for a small tip radius $R = 1.75 \mu\text{m}$ (Fig. 13), there are visible differences that do not decrease despite adopting different values of the parameter β of the Cosserat model. This issue requires further study.

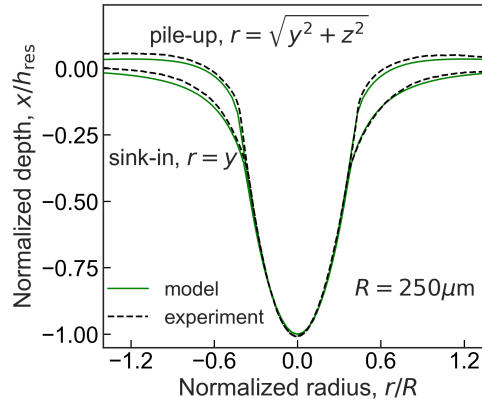


Figure 17: Distribution of the indentation depth, normalized by the maximum residual penetration depth h_{res} , along a radius r in the yz plane in two directions corresponding to the maximum pile-up or sink-in in the experiment and modelling for $R = 250 \mu\text{m}$.

Apart from the ISE as above, this paper is mainly focused on the size effect on the lattice misorientation pattern beneath the spherical indenter, both experimental and theoretical. For the purposes of numerical simulations, a more detailed parametric study, presented in Section 4.4, has been performed to select a possibly optimal value of the

coefficient β of lattice curvature energy. It has been found that $\beta = 0.03 \text{ GPa } \mu\text{m}^2$ makes the calculated dependence of maximal misorientation on tip radius qualitatively similar to that in the experiment, and is small enough not to destroy the predictive power of the PS term for hardness.

Comparing the misorientation distributions obtained from the modelling and experiment, it can be seen that in both cases the maximum value of the misorientation angle decreases with the decrease of indenter radius. In Fig. 18 the dependence of maximal misorientation angles on indenter radii for both experiment and modelling are presented. It is observed that the experimentally obtained maximal misorientation values for indenter radii ranging from $250 \mu\text{m}$ to $5.9 \mu\text{m}$ are higher, while for the smallest radius of $1.75 \mu\text{m}$ smaller than those obtained in the modelling. Nevertheless, the tendency is similar. For both experiment and modelling a sharp decrease of the maximal value of misorientation angle occurs for the indenter radius of $1.75 \mu\text{m}$, which would be more visible on a linear scale.

The experimentally obtained misorientation distribution for the largest sphere radius (Fig. 8) exhibits a triangular-shaped area with a clearly defined low-angle boundary, while this area becomes difficult to identify as the radius decreases. Such a boundary is not observed in the numerical results given in Fig. 10.

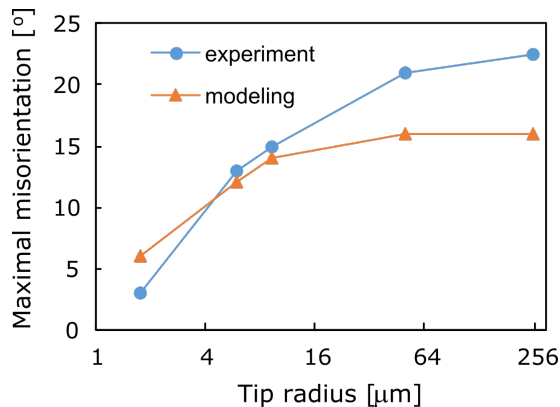


Figure 18: Dependence of maximal misorientation angle on indenter radius in the experiment and modelling.

The size effect on the Nye tensor $\boldsymbol{\alpha}$ (Eq. (16)), which is linked to the lattice curvature and usually interpreted as a geometrically necessary dislocation density tensor, has also been investigated. As shown in Fig. 9, the mean norm of the Nye tensor determined experimentally in the selected rectangle increases as the indenter radius decreases, as expected. Interestingly, the increase in the square root of the mean norm of the Nye tensor with decreasing tip radius is similar to the change in nominal hardness. A qualitatively similar trend can also be seen in Fig. 12, where the distribution of the norm of the Nye tensor for various indenter radii was determined numerically. That trend can be explained by referring to the Taylor's formula (18), where the flow stress related to hardness is proportional to the square root of the total dislocation density. Its rate is incrementally affected, according to Eq. (19), by the norm of the rate of the Nye tensor. After time integration along a nearly proportional deformation path, this incremental gradient effect manifests itself in a similar way in terms of the accumulated values. However, it should be mentioned that in the case of a deformation cycle, which is absent in the indentation test examined here, $\|\boldsymbol{\alpha}\|$ could diminish even to zero while the accumulated isotropic hardening would always be present according to the PS term in the hardening law (17).

Hence, in general, the norm of the Nye tensor itself is not a comprehensive measure of the additional hardening due to the history of plastic strain incompatibility.

5. Summary

Extensive experimental and numerical investigations of the indentation size effect (ISE) in a copper single crystal have been carried out. A spherical indentation test was performed with six different tip radii R , with the ratio of largest to smallest radius ($250 \div 1.75 \mu\text{m}$) of approximately 140. For each tip, a wide spectrum of quantities was determined that could be measured in the indentation test. In addition to the load-penetration depth curves during loading and unloading, the topography of the residual impression and the lattice rotation in the cross-section beneath the indent in the unloaded state were also examined. Such extensive studies of ISE in one material are difficult to find in the literature.

In the experimental tests, the maximum relative penetration depth h/R , which is a measure of mean strain produced by spherical indentation, was approximately equal to 0.11. So, the similar value of h/R assumed for different tip radii resulted in similar mean strains generated beneath the indenter, but lead to different strain gradients. As expected for the spherical indentation at a fixed h/R ratio, the size effect was manifested by increasing nominal hardness as the tip radius R decreased. Despite a similar strain level generated during loading, the maximal lattice rotation was the lowest for the smallest tip radius. The gradient of lattice rotation, used to determine the norm of the Nye tensor as a measure of the GND density in the selected region, shows the opposite tendency and is the greatest for the smallest tip radius. It has been shown that its square root correlates well with the increase in nominal hardness. The difference between the measured pile-up and sink-in profiles, which is a consequence of crystal anisotropy, was visibly smaller for the smallest tip radius than for the larger ones.

Numerical 3D FEM simulations were carried out using the model incorporating simultaneously two gradient-effects, within the Cosserat elastoplasticity framework with the hardening law enhanced by the slip-rate gradient term. The latter PS term was derived in the closed form without any fitting parameter, which is a distinctive feature compared to other models used in the literature. The predicted effect of tip radius on the nominal hardness turned out to be highly satisfactory compared to the measurements. It has been therefore confirmed that adding the PS gradient term to the conventional incremental hardening law provides a simple modelling tool alternative to the Nix-Gao hardening mechanism. The advantage of the current modelling approach is that the strain hardening law was fully calibrated using the stress-strain curve from the uniaxial compression test, making the above prediction of the indentation size effect on hardness automatic as it was based only on the macro-scale experiment.

In order to match the dependence of the maximal misorientation angle on the indenter radius in the modelling and experiment, the coefficient of lattice curvature energy in the Cosserat model required careful adjustment. In result, the maximal misorientation angle decreased as the indenter radius decreased, similarly as in the experiment, although full quantitative agreement was not achieved. The tendency of the increasing norm of the Nye tensor with decreasing indenter radius was also confirmed numerically.

As far as the (anisotropic) topography of the imprint surface is concerned, the pile-up and sink-in profiles predicted numerically using crystal plasticity with the calibrated power hardening law were in good agreement with those measured at the largest tip

radius. There is some discrepancy between numerical and experimental profiles for small tips, which requires further study.

6. Conclusions

The main novel conclusions of this work can be summarized as follows:

A good prediction of the experimentally observed ISE on the load-penetration depth relationship (beyond the stage of pop-in events) and nominal hardness has been obtained using the conventional power-hardening law, calibrated from a standard uniaxial compression test for a copper single crystal, enhanced with a gradient-type term that does not require any adjustable parameter. This extra term reflects the usually missing effect of the lattice spin gradient on the rate of isotropic hardening of an anisotropic crystal.

The observed distribution of lattice rotation beneath the indenter and the decrease in the rotation magnitude with decreasing indenter radius have been qualitatively modelled by adjusting the coefficient of lattice curvature energy within the adopted Cosserat elastoplasticity framework, without losing accuracy in predicting the ISE on the load-penetration depth relationship.

Acknowledgement

This work has been partially supported by the National Science Centre (NCN) in Poland through Grants No. 2014/13/B/ST8/04286 and 2018/31/B/ST8/03359. MR acknowledges the support from the European Union Horizon 2020 research and innovation program under NOMATEN Teaming grant agreement no. 857470 and from the European Regional Development Fund via the Foundation for Polish Science International Research Agenda Plus program grant no. MAB PLUS/2018/8.

References

- [1] T. T. Zhu, A. J. Bushby, D. J. Dunstan, Materials mechanical size effects: a review, *Materials Technology* 23 (2008) 193–209.
- [2] P. P. Soman, E. G. Herbert, K. E. Aifantis, S. A. Hackney, Analysis of local grain boundary strengthening utilizing the extrinsic indentation size effect, *J. Mater. Res.* 34 (2019) 2347–2369.
- [3] W. D. Nix, J. R. Greer, G. Feng, E. T. Lilleodden, Deformation at the nanometer and micrometer length scales: Effects of strain gradients and dislocation starvation, *Thin Solid Films* 515 (2007) 3152–3157.
- [4] G. M. Pharr, E. G. Herbert, Y. Gao, The indentation size effect: A critical examination of experimental observations and mechanistic interpretations, *Annu. Rev. Mater. Res.* 40 (2010) 271–92.
- [5] W. D. Nix, G. H., Indentation size effects in crystalline materials: A law for strain gradient plasticity, *J. Mech. Phys. Solids* 46 (1998) 411–425.
- [6] M. Zhao, W. S. Slaughter, M. Li, S. Mao, Material-length-scale-controlled nanoindentation size effects due to strain-gradient plasticity, *Acta Mater.* 51 (2003) 4461–4469.

- [7] D. Chicot, Hardness length-scale factor to model nano- and micro-indentation size effects.
- [8] Y. Liu, A. Ngan, Depth dependence of hardness in copper single crystals measured by nanoindentation, *Scripta Mater.* 44 (2001) 237–241.
- [9] J. G. Swadener, E. P. George, G. M. Pharr, The correlation of the indentation size effect measured with indenters of various shapes, *J. Mech. Phys. Solids* 50 (2002) 681–694.
- [10] A. Swadener, J.G. and Misra, R. Hoagland, A. Nastasi, A mechanistic description of combined hardening and size effects, *Scripta Mater.* 47 (2002) 343–348.
- [11] A. A. Elmustafa, A. A. Ananda, W. M. Elmahboub, Dislocation mechanics simulations of the bilinear behavior in micro- and nanoindentation, *J. Mater. Res.* 19 (2004) 768–779.
- [12] J. Kim, B. Lee, D. Read, D. Kwon, Influence of tip bluntness on the size-dependent nanoindentation hardness, *Scripta Mater.* 52 (2005) 353–358.
- [13] G. Feng, W. D. Nix, Indentation size effect in MgO, *Scripta Mater.* 51 (2004) 599–603.
- [14] K. Durst, B. Backes, M. Goken, Indentation size effect in metallic materials: Correcting for the size of the plastic zone, *Scripta Mater.* 52 (2005) 1093–1097.
- [15] S. Qu, Y. Huang, G. M. Pharr, K. C. Hwang, The indentation size effect in the spherical indentation of iridium: A study via the conventional theory of mechanism-based strain gradient plasticity, *Int. J. Plasticity* 22 (2006) 1265–1286.
- [16] Y. Huang, F. Zhang, K. C. Hwang, W. D. Nix, G. M. Pharr, G. Feng, A model of size effects in nano-indentation, *J. Mech. Phys. Solids* 54 (2006) 1668–1686.
- [17] W. B. Lee, Y. P. Chen, Simulation of micro-indentation hardness of FCC single crystals by mechanism-based strain gradient crystal plasticity, *Int. J. Plasticity* 26 (10) (2010) 1527–1540.
- [18] M. Liu, C. Lu, A. Tieu, Crystal plasticity finite element method modelling of indentation size effect, *Int. J. Sol. Struct.* 52 (2015) 42–49.
- [19] L. Charleux, V. Keryvi, M. Nivard, J.-P. Guin, J.-C. Sangleboeuf, Y. Yokoyama, A method for measuring the contact area in instrumented indentation testing by tip scanning probe microscopy imaging, *Acta Mater.* 70 (2014) 249–258.
- [20] Y. H. Lee, J. H. Hahn, S. H. Nahm, J. I. Jang, D. Kwon, Investigations on indentation size effects using a pile-up corrected hardness, *J. Phys. D: Appl. Phys* 41 (2008) 074027(5pp).
- [21] E. Renner, Y. Gaillard, F. Richard, F. Amiot, P. Delobelle, Sensitivity of the residual topography to single crystal plasticity parameters in berkovich nanoindentation on fcc nickel, *Int. J. Plasticity* 77 (2016) 118–140.
- [22] S. Kucharski, S. Woźniacka, Size effect in single crystal copper examined with spherical indenters, *Metall. Mater. Trans. A* 50 (2019) 2139–2154.

- [23] F. Javaid, Y. Xu, E. Bruder, K. Durst, Indentation size effect in tungsten: Quantification of geometrically necessary dislocations underneath the indentations using hr-ebstd, *Materials Characterization* 142 (2018) 39–42.
- [24] E. Demir, D. Raabe, N. Zafarani, S. Zaeferrer, Investigation of the indentation size effect through the measurement of the geometrically necessary dislocations beneath small indents of different depths using EBSD tomography, *Acta Mater.* 57 (2009) 559–569.
- [25] Y. Wang, D. Raabe, C. Klüber, R. F., Orientation dependence of nanoindentation pile-up patterns and of nanoindentation microtextures in copper single crystals, *Acta Mater.* 52 (2004) 2229–2238.
- [26] N. Zafarani, D. Raabe, R. N. Singh, F. Roters, S. Zaeferrer, Three-dimensional investigation of the texture and microstructure below a nanoindent in a Cu single crystal using 3D EBSD and crystal plasticity finite element simulations, *Acta Mater.* 54 (2006) 1863–1876.
- [27] Y. Liu, S. Varghese, J. Ma, M. Yoshino, H. Lu, R. Komanduri, Orientation effects in nanoindentation of single crystal copper, *Int. J. Plasticity* 24 (2008) 1990–2015.
- [28] H. Petryk, S. Stupkiewicz, S. Kucharski, On direct estimation of hardening exponent in crystal plasticity from the spherical indentation test, *Int. J. Sol. Struct.* 112 (2017) 209–221.
- [29] S. Kucharski, S. Stupkiewicz, H. Petryk, Surface pile-up patterns in indentation testing of cu single crystals, *Exp. Mech.* 54 (2014) 957–969.
- [30] P. Juran, P. J. Liotier, C. Maurice, F. Valiorgue, G. Kermouche, Investigation of indentation-, impact- and scratch-induced mechanically affected zones in a copper single crystal, *C. R. Mecanique* 343 (2015) 344–353.
- [31] A. J. Cackett, C. D. Hardie, J. J. H. Lim, E. Tarleton, Spherical indentation of copper: Crystal plasticity vs experiment, *Materialia* 7 (2019) 100368.
- [32] M. Demiral, A. Roy, T. El Sayed, V. V. Silberschmidt, Influence of strain gradients on lattice rotation in nano-indentation experiments: a numerical study, *Mater. Sci. Eng. A* 608 (2014) 73–81.
- [33] J. Engels, S. Gao, W. Amin, A. Biswas, A. Kostka, N. Vajragupta, A. Hartmaier, Indentation size effects in spherical nanoindentation analyzed by experiment and non- local crystal plasticity, *Materialia* (2018).
- [34] Y. F. Gao, B. C. Larson, J. H. Lee, L. Nicola, J. Z. Tischler, G. M. Pharr, Lattice rotation patterns and strain gradient effects in face-centered-cubic single crystals under spherical indentation, *J. Appl. Mech.* 82 (2015) 061007–10.
- [35] M. Rester, C. Motz, R. Pippan, Where are the geometrically necessary dislocations accommodating small imprints?, *J. Mater. Res.* 24 (2008) 648.
- [36] M. Rester, C. Motz, R. Pippan, Microstructural investigation of the volume beneath nanoindentations in copper, *Acta Mater.* 55 (2007) 6427–6435.

- [37] M. Rester, C. Motz, R. Pippan, Indentation across size scales – a survey of indentation-induced plastic zones in copper 111 single crystals, *Scripta Mater.* 59 (2008) 742–745.
- [38] T. B. Britton, H. Liang, F. P. E. Dunne, A. J. Wilkinson, The effect of crystal orientation on the indentation response of commercially pure titanium: experiments and simulations, *Proc. Phys. Soc. Lond. A* 466 (2010) 695–719.
- [39] A. Kareer, E. Tarleton, C. Hardie, S. V. Hainsworth, W. A. J., Scratching the surface: Elastic rotations beneath nanoscratch and nanoindentation tests, *Acta Mater.* 200 (2020) 116–126.
- [40] Z. Wang, J. Zhang, H. ul Hassan, J. Zhang, Y. Yan, A. Hartmaier, T. Sun, Coupled effect of crystallographic orientation and indenter geometry on nanoindentation of single crystalline copper, *Int. J. Mech. Sci.* 148 (2018) 531–539.
- [41] A. J. Wilkinson, D. Randman, Determination of elastic strain fields and geometrically necessary dislocation distributions near nanoindenters using electron back scatter diffraction, *Phil. Mag. A* 90 (2010) 1159–1177.
- [42] X. Xiao, L. Chen, L. Yu, H. Duan, Modelling nano-indentation of ion-irradiated fcc single crystals by strain-gradient crystal plasticity theory, *Int. J. Plasticity* 116 (2019) 216–231.
- [43] J. Cheng, R. Lane, M. S. Kesler, J. Brechtel, X. Hu, R. Mirzaeifar, O. Rios, A. M. Momen, K. Nawaz, Experiment and non-local crystal plasticity finite element study of nanoindentation on Al-8Ce-10Mg alloy, *Int. J. Sol. Struct.* 233 (2021) 111233.
- [44] M. J. Lewandowski, S. Stupkiewicz, Size effects in wedge indentation predicted by a gradient-enhanced crystal-plasticity model, *Int. J. Plasticity* 109 (2018) 54–78.
- [45] H. Petryk, S. Stupkiewicz, A minimal gradient-enhancement of the classical continuum theory of crystal plasticity. Part I: The hardening law, *Arch. Mech.* 68 (2016) 459–485.
- [46] C. F. O. Dahlberg, Y. Saito, M. S. Oztop, J. W. Kysar, Geometrically necessary dislocation density measurements associated with different angles of indentations, *Int. J. Plasticity* 54 (2014) 81–95.
- [47] A. Sarac, M. S. Oztop, C. F. O. Dahlberg, J. W. Kysar, Spatial distribution of the net Burgers vector density in a deformed single crystal, *Int. J. Plasticity* 85 (2016) 110–129.
- [48] S. Stupkiewicz, H. Petryk, A minimal gradient-enhancement of the classical continuum theory of crystal plasticity. Part II: Size effects, *Arch. Mech.* 68 (2016) 487–513.
- [49] M. Ryś, S. Stupkiewicz, H. Petryk, Micropolar regularization of crystal plasticity with the gradient-enhanced incremental hardening law, *Int. J. Plasticity* 156 (2022) 103355.
- [50] A. C. Fischer-Crips, *Nanoindentation*, Springer, New York, 2004.

- [51] J. R. Morris, H. Bei, G. M. Pharr, E. P. George, Size effects and stochastic behavior of nanoindentation pop in, *Phys. Rev. Lett.* 106 (2011) 165502–1–165502–4.
- [52] X. Xiao, S. Li, L. Yu, Effect of irradiation damage and indenter radius on pop-in and indentation stress-strain relations: Crystal plasticity finite element simulation, *Int. J. Mech. Sci.* 199 (2021) 106430–1–106430–15.
- [53] M. Liu, A. K. Tieu, C. Lu, H. Zhu, G. Deng, A crystal plasticity study of the effect of friction on the evolution of texture and mechanical behaviour in the nano-indentation of an aluminium single crystals, *Comp. Mat. Sci.* 81 (2014) 30–38.
- [54] B. Beausir, J. Fundenberger, Analysis tools for electron and x-ray diffraction, ATEX-software, www.atex-software.eu, Université de Lorraine-Metz (2017).
- [55] W. Pantleon, Resolving the geometrically necessary dislocation content by conventional electron backscattering diffraction, *Scripta Mater.* 58 (2008) 994–997.
- [56] S. Forest, Some links between Cosserat, strain gradient crystal plasticity and the statistical theory of dislocations, *Phil. Mag.* 88 (30-32) (2008) 3549–3563.
- [57] N. M. Cordero, A. Gaubert, S. Forest, E. P. Busso, F. Gallerneau, S. Kruch, Size effects in generalised continuum crystal plasticity for two-phase laminates, *J. Mech. Phys. Solids* 58 (11) (2010) 1963–1994.
- [58] E. Kröner, *Kontinuumstheorie der versetzungen und eigenspannungen*, Springer, 1958.
- [59] J. F. Nye, Some geometrical relations in dislocated crystals, *Acta Metall.* 1 (1953) 153–162.
- [60] G. I. Taylor, The mechanism of plastic deformation of crystals. Part I. Theoretical, *Proc. R. Soc. Lond. A* 145 (1934) 362–387.
- [61] U. F. Kocks, H. Mecking, Physics and phenomenology of strain hardening: the FCC case, *Progress Mater. Sci.* 48 (2003) 171–273.
- [62] J. Korelc, U. Šolinc, P. Wriggers, An improved EAS brick element for finite deformation, *Comp. Mech.* 46 (4) (2010) 641–659.
- [63] W. R. Inc., *Mathematica, Version 13.2*, champaign, IL, 2022.
URL <https://www.wolfram.com/mathematica>
- [64] J. Korelc, P. Wriggers, *Automation of Finite Element Methods*, Springer, 2016.
- [65] E. Schmid, W. Boas, *Plasticity of crystals*, Hughes, London, 1950.
- [66] G. Simmons, H. Wang, *Single crystal elastic constants and calculated aggregate properties*, M.I.T. Press, Cambridge, MA, 1971.
- [67] M. Sauzay, L. P. Kubin, Scaling laws for dislocation microstructures in monotonic and cyclic deformation of fcc metals, *Progress Mater. Sci.* 56 (2011) 725–784.
- [68] J. W. Hutchinson, Bounds and self-consistent estimates for creep of polycrystalline materials, *Proc. R. Soc. Lond. A* 348 (1976) 101–127.